Chapter 6

Investigation of time-averaged acoustic streaming using a multiple stack model

In this chapter, the system of numerically modelling thermoacoustic couples developed in Chapter 3 is applied to investigate interesting outcomes from experimental studies in the literature. Similar to the method described in Chapter 5, the numerical model is again perturbed in an attempt to capture flow features prevalent in realised stacks. For the first time in this thesis, multiple stack plates are considered.

Acoustic streaming, a phenomenon discussed in Section 2.3.3, is explored using an expanded numerical model which seeks to model multiple stack plates at various drive ratios. For this expanded domain, mean gas pressures are also increased to 1 bar (near atmospheric) to encourage acoustic streaming patterns in the model which are possibly greater in scale than the stack dimensions.

Section 6.1 describes the expanded modelspace and new operating conditions

used in this study. In Section 6.2 the results of the simulations are presented and the outcomes in terms of temperature fields, acoustic streaming and influence of stack materials are discussed.

6.1 Modelspace and operating conditions

Acoustic streaming within thermoacoustic stacks is explored using a numerical model which extends from the centreline of the resonator to the internal wall, incorporating multiple stack plates. A sketch of the domain under consideration in this study is shown in Figure 6.1. The four-plate model is designed to investigate suspicions that acoustic streaming within stack regions in standing-wave devices may be attributed to differences in flow resistance between stack channels in the axial centre and the near-wall regions. Where possible, the geometry of each individual stack plate will be the same as the Rectangular model presented in Chapter 5.
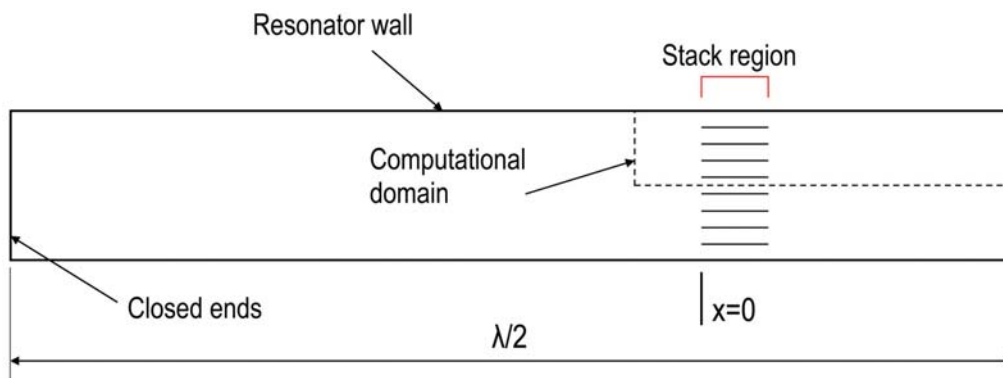

Figure 6.1: Sketch of the computational domain of the expanded thermoacoustic couple model within a half wavelength standing-wave resonator.

Figure 6.2 shows the expanded computational domain with greater detail. The computational domain is effectively eight times greater in the transverse (y) direction than the domain used in Chapters 4 and 5, and 'extends' to the wall of the resonator. For Runs 1 to 5 where $y_0=0.008$m, the model is now $y_{CV}=8y_0=0.064$m wide in the transverse dimension but its total length L_{CV} of 1.476m is retained.

Symmetrical boundary conditions on the lower edge of the domain ($y=0$) are retained. The resonator wall is considered to be insulated, with $dT/dy=0$ on this boundary. The flow resistance experienced by the fluid is higher at locations within a viscous penetration depth δ_v of the walls of the resonator and outermost stack plates than on the central axis of the resonator. This difference is expected to create a flow imbalance across the stack face. The flow imbalance, should it develop, is therefore expected to create a non-zero time-averaged flow path greater in size than one single stack channel.
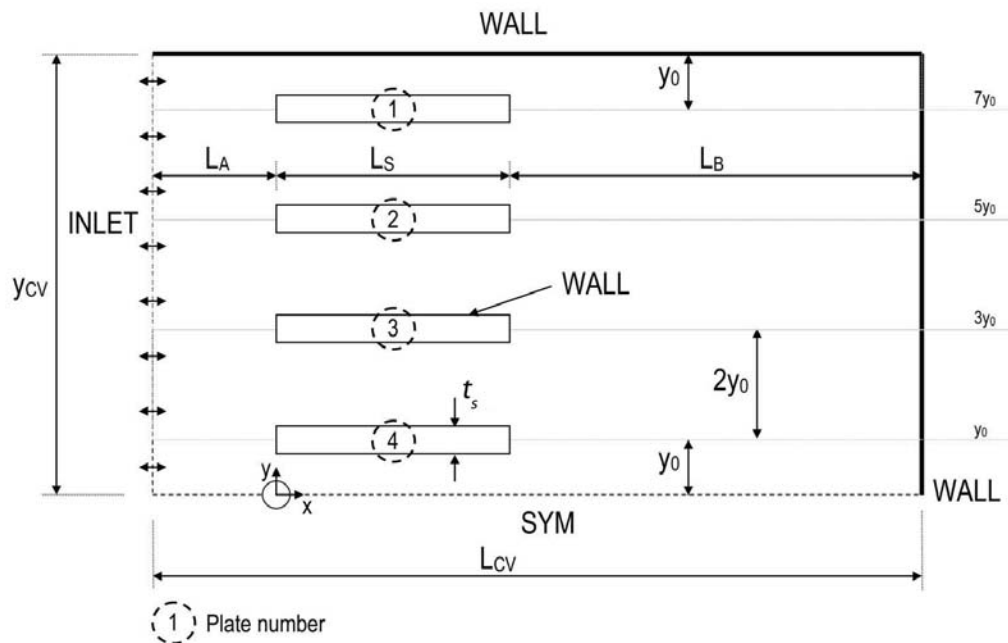

Figure 6.2: Sketch of boundary conditions and major geometry features of the expanded thermoacoustic couple model.

Table 6.1 lists the operating conditions used in this study. In Runs 1 and 2, the expanded model is driven at drive ratios of 1.7% and 6.8%, using helium at an ambient pressure ρ_m of 10kPa, for comparison with the results of Chapters 4 and 5. Each stack plate is individually assessed with regard to the time-averaged heat flux and cooling capacity. Time-averaged temperature gradients are taken on $y=0$, $y=0.5y_0$, $y=4y_0$, and $y=7.5y_0$, to investigate the influence of acoustic streaming on

temperatures throughout selected stack channels. Gravity or buoyancy effects were not modelled.

Table 6.1: Operating conditions considered in Chapter 6. All runs model helium as the working fluid.

Run	p_m (bar)	f (Hz)	$t_s/\delta_{\kappa m}$	$\lvert p_1 \rvert / p_m$ (%)
1	0.1	100	0.99	1.70
2	0.1	100	0.99	6.80
3	1.0	100	3.2	1.70
4	1.0	100	3.2	3.40
5	1.0	100	3.2	5.10
6	1.0	100	1.0	1.70
7	1.0	100	1.0	3.40
8	1.0	100	1.0	5.10

The four plates are labelled from 1 to 4, with Stack Plate 1 located near the resonator wall and Stack Plate 4 located near the axis of the resonator. For Runs 1 to 5, Stack Plate 1 is located on $y=0.056$m and Stack Plate 4 is located on $y=0.008$m. The four plates are each set at a fixed pitch of $2y_0$. Rectangular edge shapes were modelled to provide comparison with the results of Chapter 4 and 5, and also exacerbate the potential for flow recirculation.

Runs 6 to 8 use identical operating and boundary conditions to Runs 3 to 5 respectively, with the exception that the ratio of stack plate thickness to mean thermal penetration depth $t_s/\delta_{\kappa m}$ is reduced from 3.2 to approximately one. As per the discussion in Section 4.1.5, this enables closer representation of a realised stack.

6.2   Results and discussion

Discussion of the results obtained in this chapter are presented in the following subsections, in terms of flow structures (Section 6.2.1), heat transportation (Section 6.2.2) and temperature fields (6.2.3).

6.2.1 Flow structures

Figure 6.3(a) presents the distribution in streaming Reynolds number $N_{R,S} = |u_1|^2/(\upsilon\omega)$ at t=0.21s for a drive ratio of 1.7% at a mean pressure of 1 bar. At this point in time, the free stream velocity magnitude is effectively at its peak within its cycle, and flow is predominantly rightward. The discussion presented in Section 4.1.3.1 placed an upper limit of $N_{R,S}^c = 40{,}000$. In presenting $N_{R,S}$ values at a time instant in which the free stream velocity is highest, Figure 6.3(a) demonstrates compliance with the criterion $N_{R,S} \ll N_{R,S}^c$ for Runs 1 and 3.

Run 2 which used a drive ratio of 6.8%, exceeded the $N_{R,S} \ll N_{R,S}^c$ criterion in each stack channel, particularly in regions immediately downstream of the leading plate edge. Run 2 was developed for comparison with Run 20 of Chapter 4, which uses the same operating conditions and blockage ratio, however exceedance of the $N_{R,S}^c$ criterion prevents this. Interestingly, the maximum value of $N_{R,S}$ for Run 2 was $\approx$75,500, or just over twice the value obtained using the half-plate model in Chapter 4. It will be shown later in this chapter that this exceedance is due to second-order acoustic streaming and flow instabilities.

Figure 6.3(b) presents the distribution in streaming Reynolds number $N_{R,S}$ at t=0.21s for a drive ratio of 5.1%. This figure shows that at this instant in time, the streaming Reynolds number exceeds the set criterion is at several locations inside the stack region near Stack Plate 2. The consequence of this exceedance is that turbulent flow structures or significant non-linear effects (Merkli & Thomann 1975a) are expected to occur qualitatively but may not be accurately captured by the numerical model. In other words, qualitative behaviour is expected to be representative, but quantitative values may be questionable. The highest value of $N_{R,S}$ obtained in Run 5 using a drive ratio of 3.4% was $28{,}200 \approx (167)^2 < N_{R,S}^c$. In Run 8 with a drive ratio of 5.1% and t_s/δ_κ equal to 1, the highest value of $N_{R,S}$
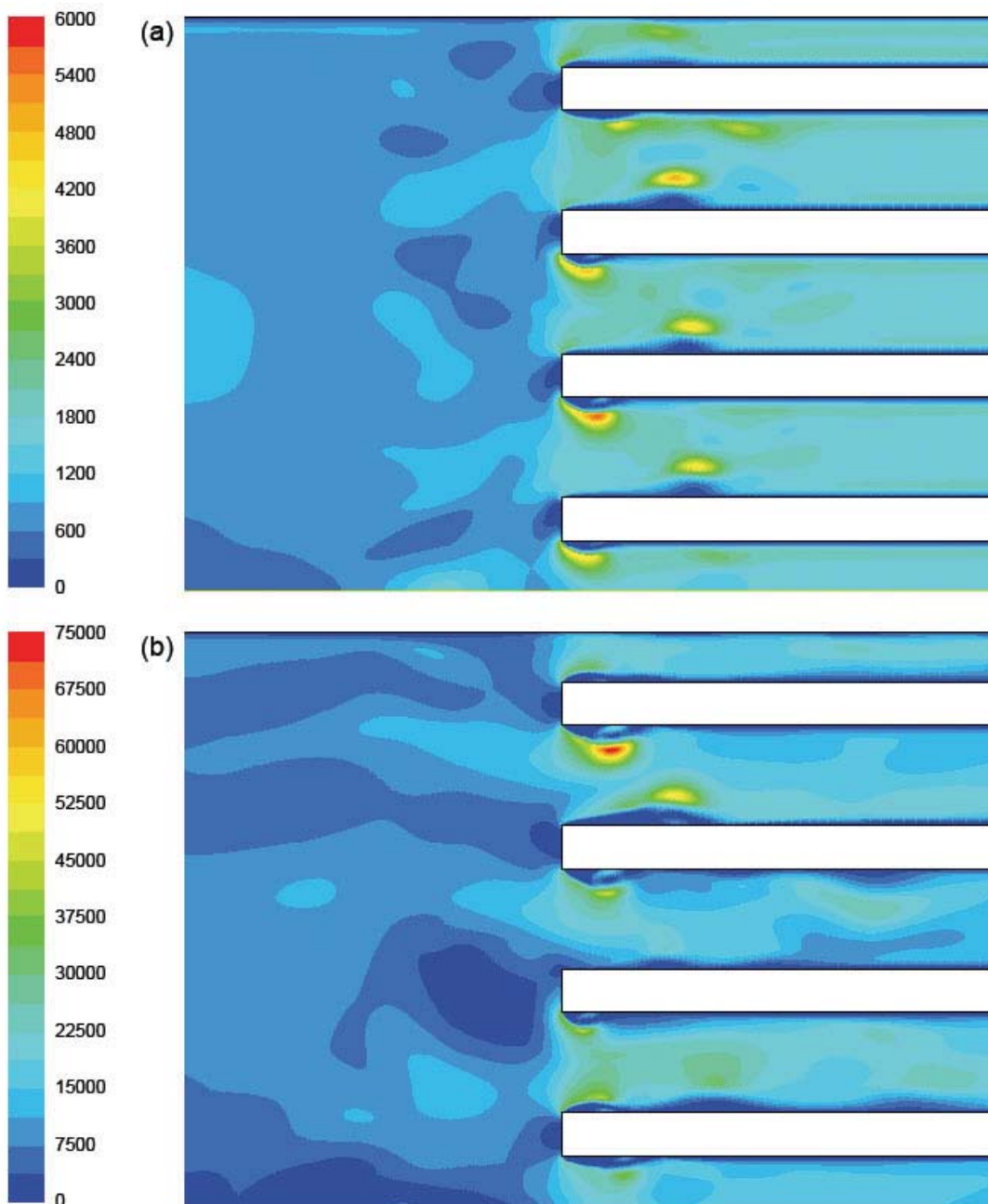
Figure 6.3: Distribution of streaming Reynolds number $N_{R,S}$ at t=0.21s using a drive ratio of (a) 1.7% (Run 2) and (b) 5.1% (Run 4). p_m= 1 bar.

obtained was $34{,}000 \approx (184)^2 < N_{R,S}^c$.

Figure 6.4 presents pathlines for Run 4 at time t=0.21s (same time instant as Figure 6.3(b)), where the flow is rightward and its magnitude is near maximum in the cycle. At the left end of the stack plates near x=0 (Figure 6.4(a)), small
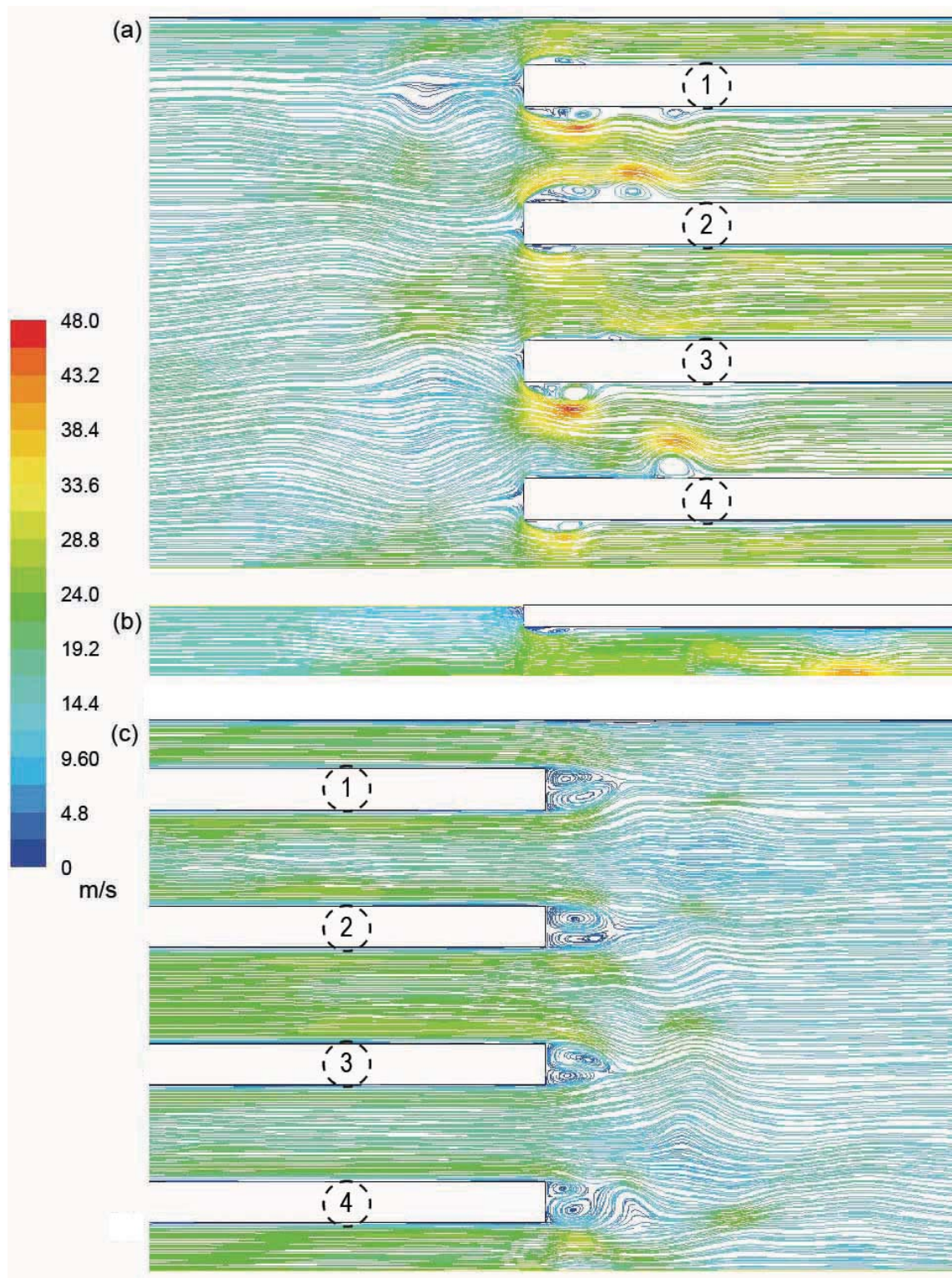
Figure 6.4: Pathlines for the (a) left stack plate ends for Run 4, (b) left end of Run 5 of Appendix D.3, and (c) right stack plate ends for Run 4, t=0.21s. Pathlines are coloured by velocity magnitude (m/s). Stack plate numbers are annotated.

vortices are shown to have developed inside the stack region and downstream of the plate edges. Note that these vortices primarily occur in conjunction with higher flow velocities in the channels between Stack Plates 1 and 2, and Stack Plates 3 and 4. The pathlines left of the stack region in Figure 6.4(a) suggest that whilst flow entering the top, central and bottom stack channels (i.e. above Stack Plate 1, between Stack Plates 2 and 3 and below Stack Plate 4) is relatively undisturbed, there is increased flow resistance in the other two stack channels. The increased flow resistance is evident in the increased velocity differentials between outside and inside the stack region at these two stack channels.

Appendix D presents several small studies using the numerical model developed in Chapter 3. In Appendix D.3, the performance of various stack plate materials under identical acoustic conditions is compared. Run 5 of Appendix D.3 uses the same material properties and flow conditions as Run 4 in this chapter. It uses the same materials and operating conditions but considers only one half of a stack pore.

The result obtained from Run 5 of Appendix D.3 is similar but not representative of the result obtained in Run 4. A small recirculation zone immediately downstream of the stack plate edge is common to both Stack Plate 4 of Run 4 and the plate edge modelled in Run 5 of Appendix D.3. However, the distribution of velocity magnitude inside the stack region at this timeframe is different between each model. The modelspace used in Run 5 of Appendix D.3 assumes that flow and temperature fields through each stack pore are symmetrical and periodic on a plate to plate basis. Figures 6.3 and 6.4 show this to be unlikely with a multiple stack plate model. Further to this, the flow rate below Stack Plate 4 of Run 4 in Figure 6.4(a) is so much higher than that below the stack plate in Run 5 of Appendix D.3 (Figure 6.4(b)) that fluid flow from elsewhere in the domain (in the form of acoustic streaming) must be involved. This instability is evident even at

low drive ratios.

The lower flow velocities in stack channels between Stack Plates 1 and 2, and Stack Plates 3 and 4 (as shown Figure 6.4(c)) provides further confirmation of non-uniform flow across the stack face. Trailing edge vortices downstream of the stack plate edges in Figure 6.4(c) are also asymmetrical and demonstrate flow instability, even during phases of flow maxima.

Figures 6.5 and 6.6 compare pathlines obtained near the right end of the stack region for Runs 3 and 4, over the time period t=0.2s to t=0.205s. Ten images for each Run are presented, in $18°$ phase increments, showing in detail the flow structure as the free stream velocity decelerates from a rightward flow maximum (Figures 6.5(a) to 6.5(e)) and then accelerates from zero to a leftward flow maximum (Figures 6.6(a) to 6.6(e)).

Figure 6.5 demonstrates the significant increase in flow instability outside the stack region achieved in doubling the drive ratio DR from 1.7% to 3.4%. Due to higher velocity amplitudes, the steady laminar separation flows downstream of stack plate edges transition into unsteady laminar separation flows. Pairs of trailing edge vortices developed at the edges of the stack plates, which are relativelely symmetrical for DR=1.7%, appear as asymmetrical structures for DR=3.4% in Figures 6.5(a) and 6.5(b). Instead of being attached and stable 'separation bubbles' in the case of Run 3 (DR=1.7%), these vortices roll up the shear layer flow, 'shed' from the plate edges and move downstream, with flow immediately downstream of each trailing edge appearing as von Kármán vortex shedding trails. Figures 6.5(c) to 6.5(d) show that to the right of the stack region, the pathlines are more streamlined and less complicated as the prevailing flow decelerates. In Figure 6.5(e), when the flow is nearly stationary, the instabilities
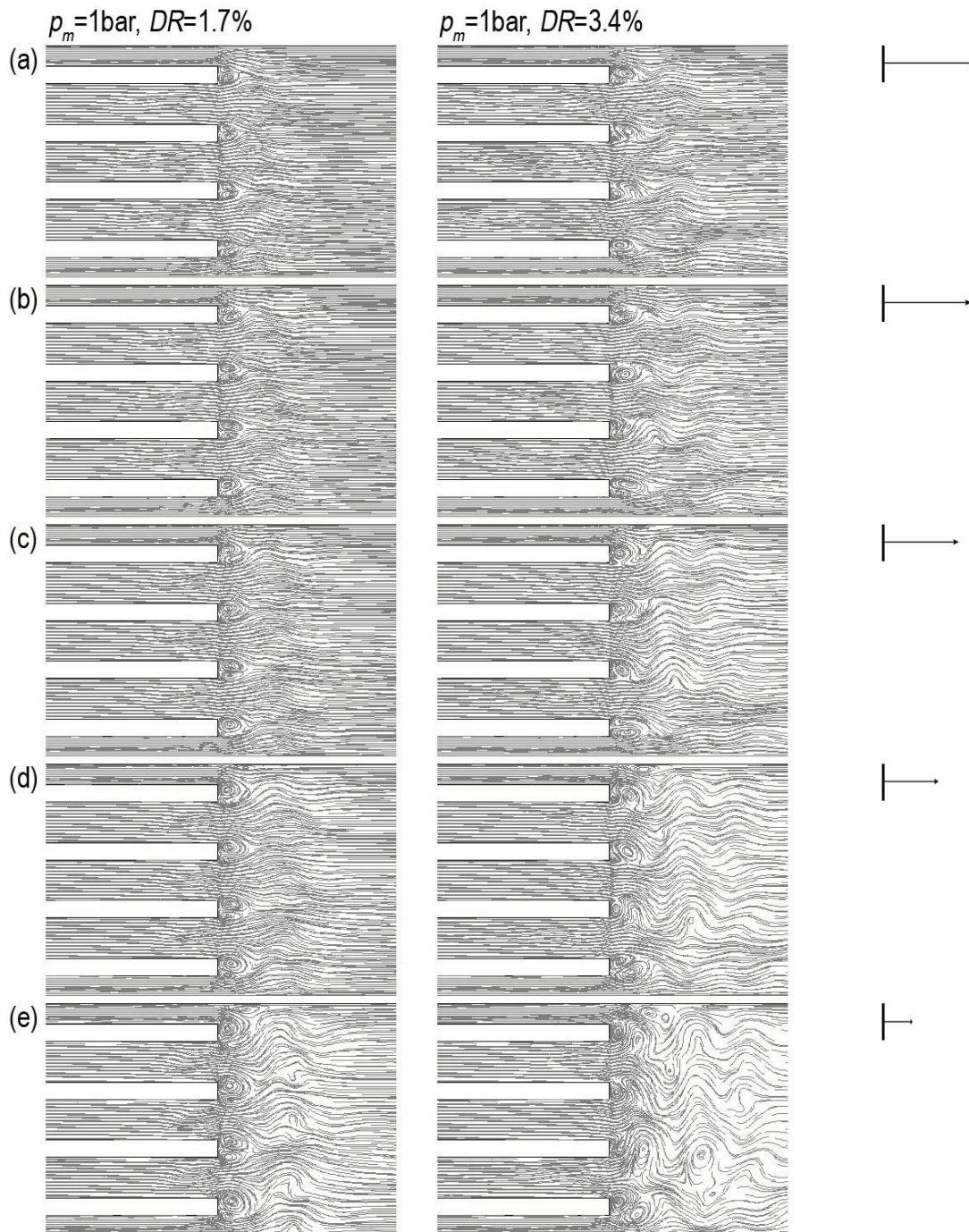
Figure 6.5: Comparison of pathlines on the right end of Runs 3 (left) and 4 (right). Phase is (a) $\phi=0°$, (b) $\phi=18°$, (c) $\phi=36°$, (d) $\phi=54°$ and (e) $\phi=72°$. Free stream velocity direction and magnitude are indicated on the right of each figure.
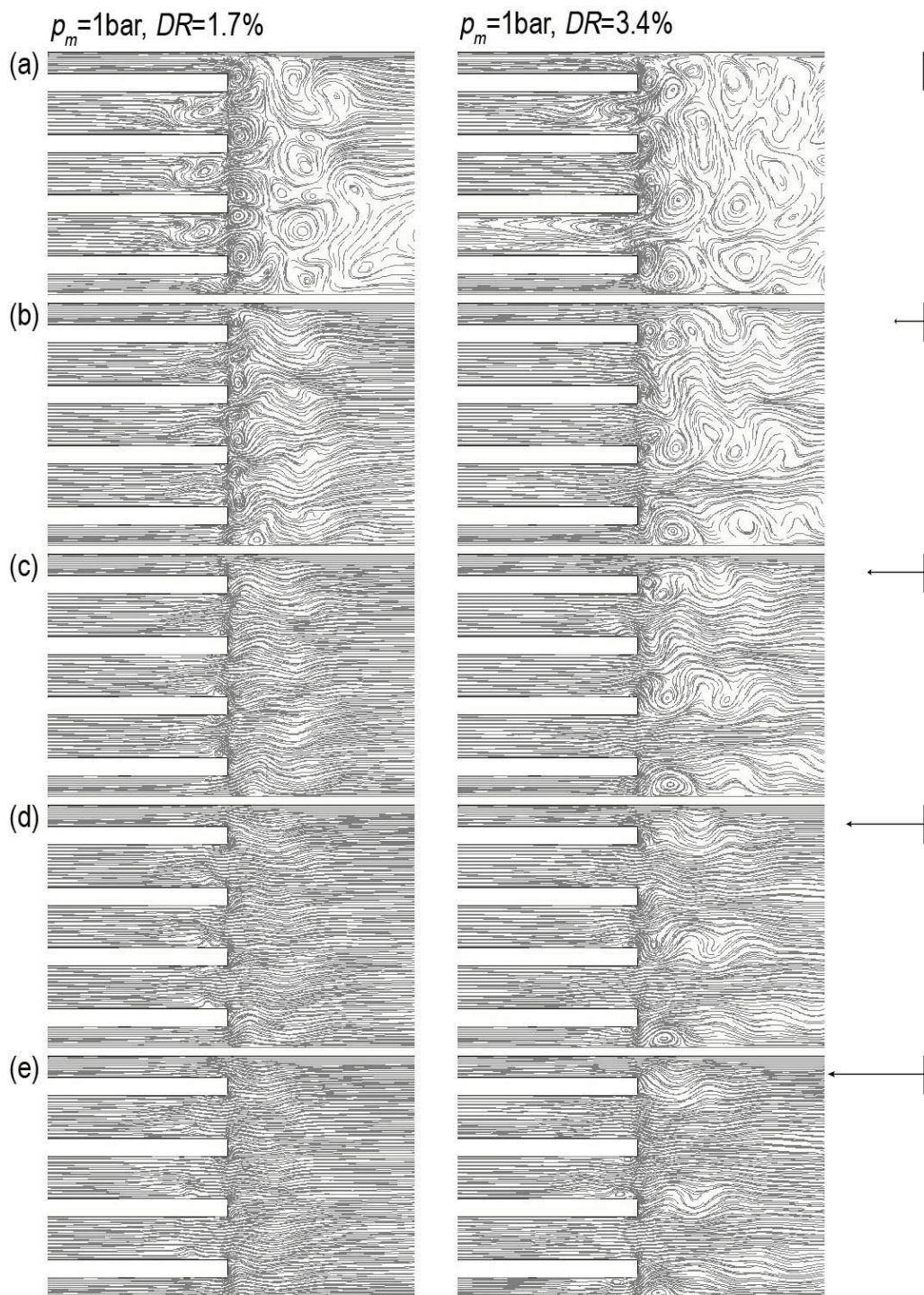
Figure 6.6: Comparison of pathlines on the right end of Runs 3 (left) and 4 (right). Phase is (a) $\phi=90°$, (b) $\phi=108°$, (c) $\phi=126°$, (d) $\phi=144°$ and (e) $\phi=162°$. Free stream velocity direction and magnitude are indicated on the right of each figure.

in flow field for DR=3.4% are most dramatic as each vortex trail slows and collapses.

The increased rate of gas recirculation in Run 4 over Run 3 is again shown through comparison of pathlines within the stack region at ϕ=90°, at a point in time where the free stream velocity is zero (Figure 6.6(a)). The flow structure appears similar in the stack channels between Stack Plates 1, 2, 3 and 4 for Run 3, whereas there is variation in pathlines plotted at the same time instant for Run 4. The flow fields between Stack Plates 1 and 2, and 3 and 4, are distinguished from the flow field in between Stack Plates 2 and 3, which is relatively streamlined. Acoustic streaming around the stack region is believed to circulate 'into' this channel at this phase in the cycle. There variation in instability between Runs 3 and 4 is quite evident outside the stack region in Figure 6.6(c). Figures 6.6(b) to 6.6(d) show the collapse of vortex trails as the gas accelerates leftward. Apart from several small recirculation zones developing on the inside edge of the stack plates, the flow field for Run 3 shown in Figure 6.6(d) is relatively featureless when compared to Run 4.

It is unclear whether the undesirable generation and later interaction of von Kármán vortex trails with Rayleigh gas streams at distance from the stack region might be suppressed with the addition of heat exchanger plates at each end of the stack plates, as per convention in practical thermoacoustic systems. Rounding the edges of the stack plates seems to be a potentially feasible method to significantly reduce the size of the separation zone developing immediately downstream of the plate edge.

Figure 6.7 presents a contour plot of the mean x velocity $\langle u \rangle_t$ for Runs 1, 3 and 4, as well as Run 17 of Chapter 4 (to enable comparison with Run 1). The stack plates are coloured black for clarity. The visible differentials in $\langle u \rangle_t$ are

indicators of flow recirculation and hence acoustic streaming (which is often defined as time-averaged non-zero mean flow). For a mean pressure of 0.1 bar (Runs 1 and 2), the distribution in $\langle u \rangle_t$ is reasonably uniform and appears periodic near Stack Plates 2, 3 and 4. The magnitude of acoustic streaming near Stack Plate 1 is slightly less than near the other three plates, and this is attributed to the edge wall condition and hence greater flow resistance through the pore above Stack Plate 1.

The distribution in mean x velocity is in excellent agreement near Stack Plate 4 of Run 1 shown in Figure 6.7(a) and the single plate simulation of Run 17 of Chapter 4 shown in Figure 6.7(b). Therefore, the assumption of symmetric or periodic flow regimes between stack channels at a mean pressure of 0.1bar as used by Ishikawa & Mee (2002), Cao et al. (1996) and the studies presented in Chapters 4 and 5 is reasonable according to Figure 6.7.

For a mean pressure of 1 bar (Figure 6.7(c)), a large recirculation, at a scale similar to the width of the computational domain, is seen to the far left of the figure, with smaller recirculation zones closer to the stack plate edges. Across the stack plate edges, flow entering the stack is expected to be concentrated in vectors oblique to the axis of each stack pore. Flow exiting the stack is expected to be concentrated near the plate edge but parallel to the stack pore. Inside the stack region, and confirming the result indicated by Figure 6.3, Figure 6.7(c) shows zones of recirculation inside each stack pore of far greater magnitude than that observed for p_m=0.1bar.

Figures 6.7(d) and 6.8 present the time-averaged x-velocity $\langle u \rangle_t$ of Run 4 for the left end of the stack and the entire stack region respectively. There is clearly significant variance in the flow structure from increasing the mean pressure p_m from 0.1 bar to 1 bar, and also from increasing the drive ratio from 1.7% to 3.4% at the
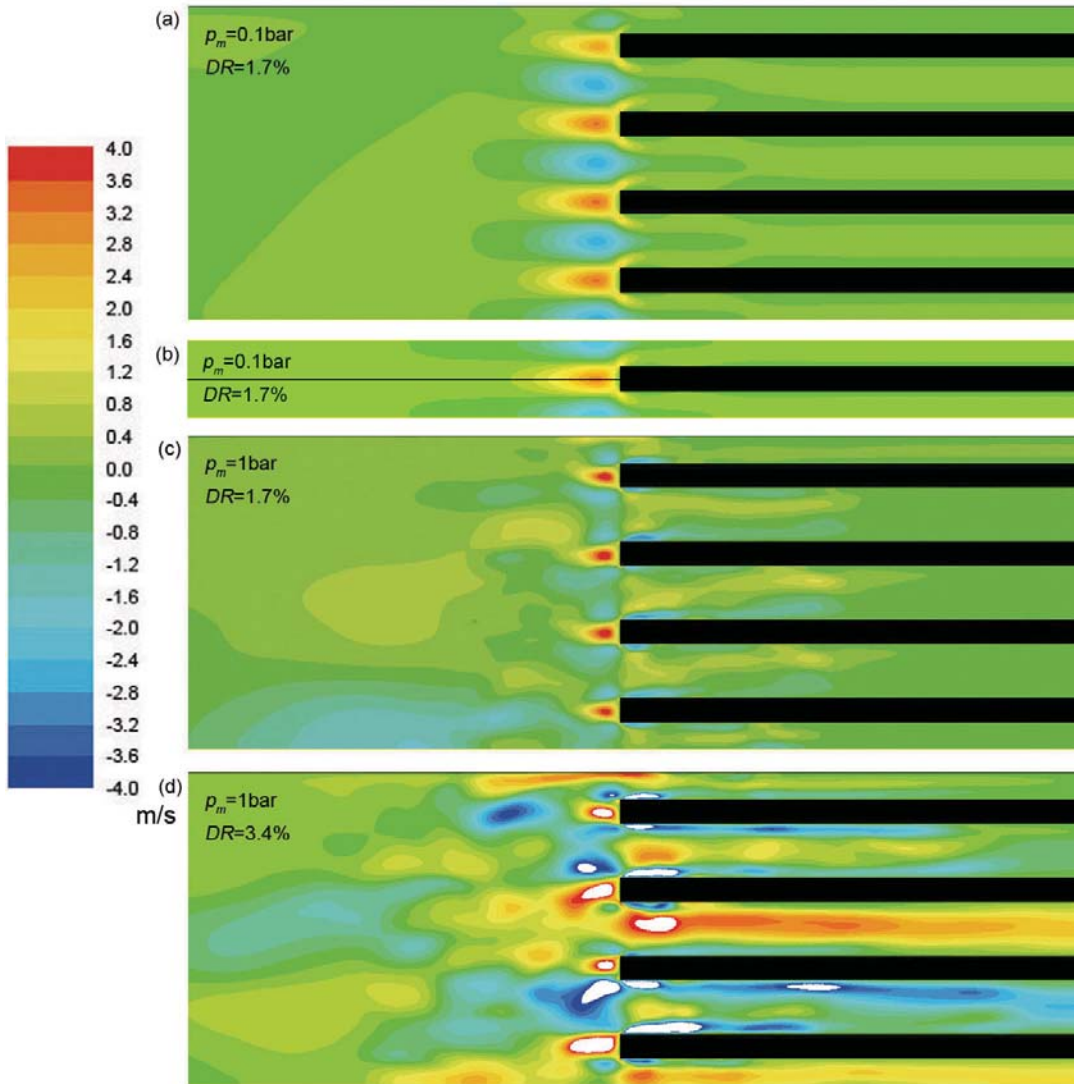
Figure 6.7: Mean x velocity $\langle u \rangle_t$ for (a) Run 1, (b) Run 17 of Chapter 4 (result mirrored across stack plate mid-thickness), (c) Run 3 and (d) Run 4. Areas not coloured (white) are outside the range -4 to 4 m/s. Positive $\langle u \rangle_t$ is to the right of figure.
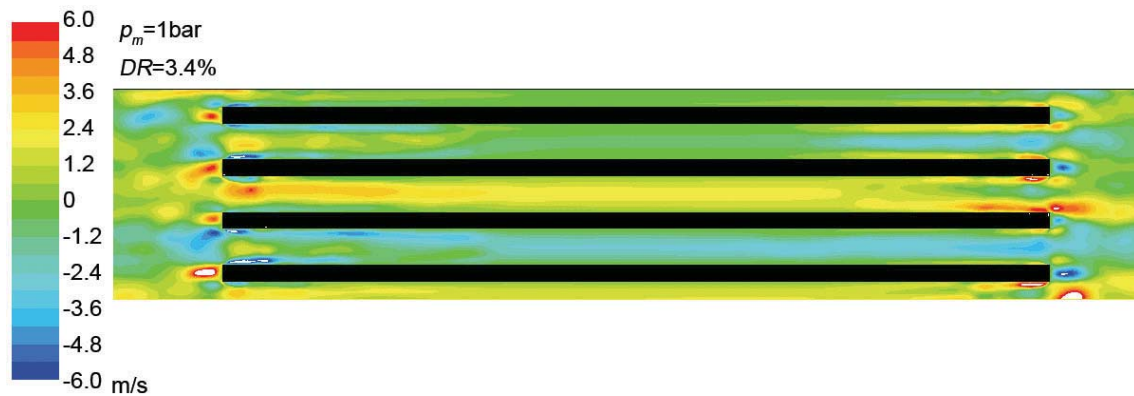
Figure 6.8: Mean x velocity $\langle u \rangle_t$ for Run 4, showing entire stack region. Areas not coloured (white) are outside the range -6 to 6 m/s. Positive $\langle u \rangle_t$ is to the right of figure.

higher mean pressure. Figures 6.7(d) and 6.8 show that at $DR=3.4\%$ and $p_m=1$ bar, $\langle u \rangle_t$ is non-uniform and potentially unstable. The time-averaged x-velocity $\langle u \rangle_t$ is predominantly rightward (positive) in the space between Stack Plates 2 and 3 and below Stack Plate 4, but strongly leftward (negative) in the spaces between Stack Plates 1 and 2 and to a larger degree, Stack Plates 3 and 4. This demonstrates that acoustic streaming loops which *fully enclose* Stack Plates 2, 3 and 4 are present. For this simulation, acoustic streaming is seen to be anticlockwise around Stack Plates 2 and 4, but clockwise around Stack Plate 3. It is interesting to note that similar patterns in $\langle u \rangle_t$ were not found for Run 3, where the drive ratio was smaller (1.7%).

The recirculation patterns which develop well outside the stack region are described as a form of *Rayleigh* streaming (Swift 2002, p177). Within the stack region a different mode of acoustic streaming has been demonstrated to occur here and cannot be readily assigned to an existing classification of acoustic streaming. The source of flow instability is attributed to the interaction of *jet-driven* streaming (Swift 2002, p187) exiting the stack region with Rayleigh streaming at distance from the stack region. At phases in which fluid accelerates to re-enter the stack region, the flow is still unstable and fluid is unequally divided amongst the stack

pores. On this basis, as the momentum of fluid across the stack channels is then unequal, the magnitude of jet flows exiting the other side will be unequal, inducing higher rates of flow recirculation.

Figures 6.9 and 6.10 present the normalised mean x velocity versus normalised y position on the line of stack midsection at $x=L_S/2$ for $t_s/\delta_{\kappa m}$ equal to 3.2 and unity respectively. Time-averaged velocity in the y direction, $\langle v \rangle_t$, at this axial position is several orders of magnitude less than $\langle u \rangle_t$ and therefore the flow at this position is considered axial. In these figures, Plate 4 is located on $y=y_0$ with Plate 1 located on $y=7y_0$. Figure 6.9 shows that time-averaged velocities at drive ratios above 3% are significantly higher for $t_s/\delta_{\kappa m}=3.2$. Similar increases in normalised $\langle u \rangle_t$ were not found for Runs 7 and 8. This discrepancy is attributed to utilising plates thinner than the viscous penetration depth.

The variation in $\langle u \rangle_t/u_{rms}$ between the stack channels indicates streaming which loops around each solid structure. The direction of streaming patterns is reversed between Runs 4 and 5, without $\langle u \rangle_t/u_{rms}$ equal to zero in the stack channels adjacent to Stack Plates 3 and 4. Runs 6 to 8 show slight variation in $\langle u \rangle_t/u_{rms}$ between each Stack Plate, with $\langle u \rangle_t/u_{rms}$ positive in the centre of all channels adjacent to Stack Plates 2, 3 and 4, but negative on y/y_0 values near the surfaces of each plate. This indicates that in the stack midsection, time-averaged flow is rightward in the centre of most stack channels but leftward near to the plate surfaces, creating flow circulation within the stack channel. Values of $\langle u \rangle_t/u_{rms}$ are significantly higher in the two channels centred on y/y_0 equal to two and six, than the others. Therefore, there is some acoustic streaming that loops several stack plates but not at a magnitude near that of Runs 3 to 5 where the ratio t_s/δ_v is several times higher.

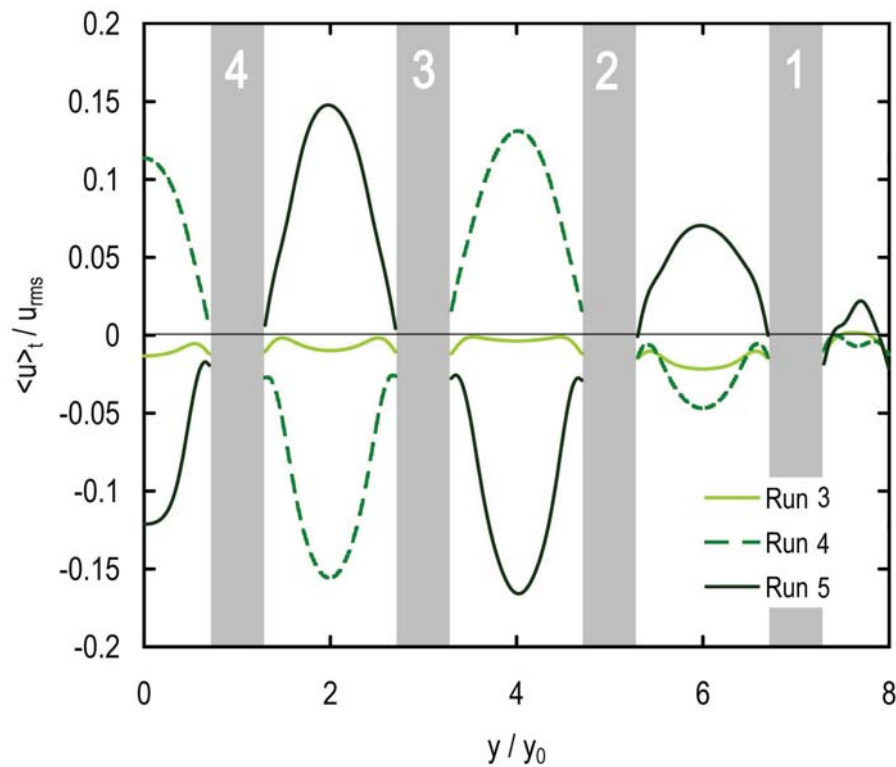The results demonstrate a dramatic shift in the rate of acoustic streaming and

Figure 6.9: Normalised mean x velocity versus normalised y position on line of stack midsection ($x=L_S/2$) for Runs 3 to 5 ($t_s/\delta_{\kappa m}=3.2$). Positive $\langle u \rangle_t/u_{rms}$ is rightward. Labelled grey shaded areas represent each of the four stack plates.

flow instability between Run 3 ($p_m=1$ bar, $DR=1.7\%$) and Run 5 ($p_m=1$ bar, $DR=5.1\%$). The experimental study of Berson & Blanc-Benon (2007, Figure 2) also demonstrated a significant increase in flow instability between results obtained using atmospheric air at $DR \approx 1\%$ and $DR \approx 5\%$. Berson & Blanc-Benon cite vortex shedding from the plate edges as a phenomenon which impacts upon the effective rate of transfer between the stack plate material and the working gas. Further to the study of Berson & Blanc-Benon, the following section quantifies the impact of acoustic streaming upon the performance of each stack plate.

6.2.2 Heat transportation

Figures 6.11 and 6.12 compare the time-averaged rate of heat transfer of Run 1 with Run 1 of Chapter 5. These simulations are intended to investigate whether the expanded solution domain leads to results that are significantly different from
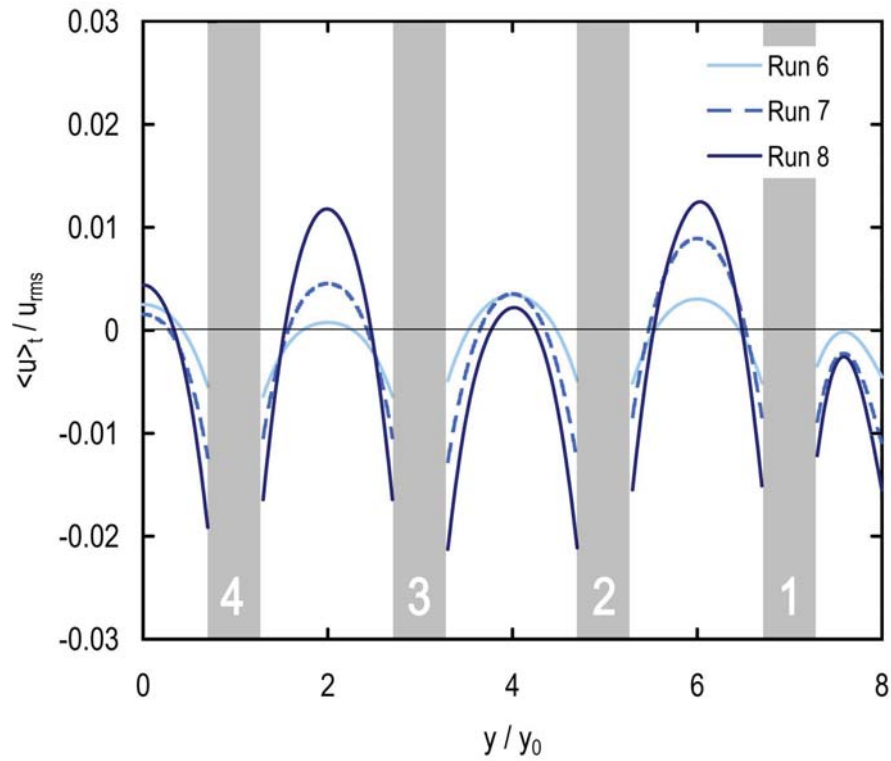
Figure 6.10: Normalised mean x velocity versus normalised y position on line of stack midsection ($x=L_S/2$), for Runs 6 to 8 ($t_s/\delta_{\kappa m}=1.0$). Positive $\langle u \rangle_t/u_{rms}$ is rightward. Labelled grey shaded areas represent each of the four stack plates.

studies in previous chapters. As shown in Figure 6.11, the time-averaged rate of heat transfer across the stack plate for a single plate model is similar to that calculated for both sides of all four plates in the expanded model. Further to this, the time-averaged rate of heat transfer across the stack plate for a single plate model is closest to the result obtained on Stack Plates 2, 3 and 4, which are located further from the resonator wall than Stack Plate 1. The outcome from this comparison is that the assumption of stack periodicity in the single plate model as described in Chapter 3 is an effective technique in reducing the size of the computational domain required.

Figure 6.12 clearly shows two different curves for Stack Plate 1, one for each side of the plate. Interestingly, the plate side which generates more desirable values of the time-averaged transverse heat flux $\left\langle \dot{h}_y \right\rangle_t$ is the plate edge on $y=0.0584$m, or the side closest to and facing the resonator wall. It is possible that the reduction
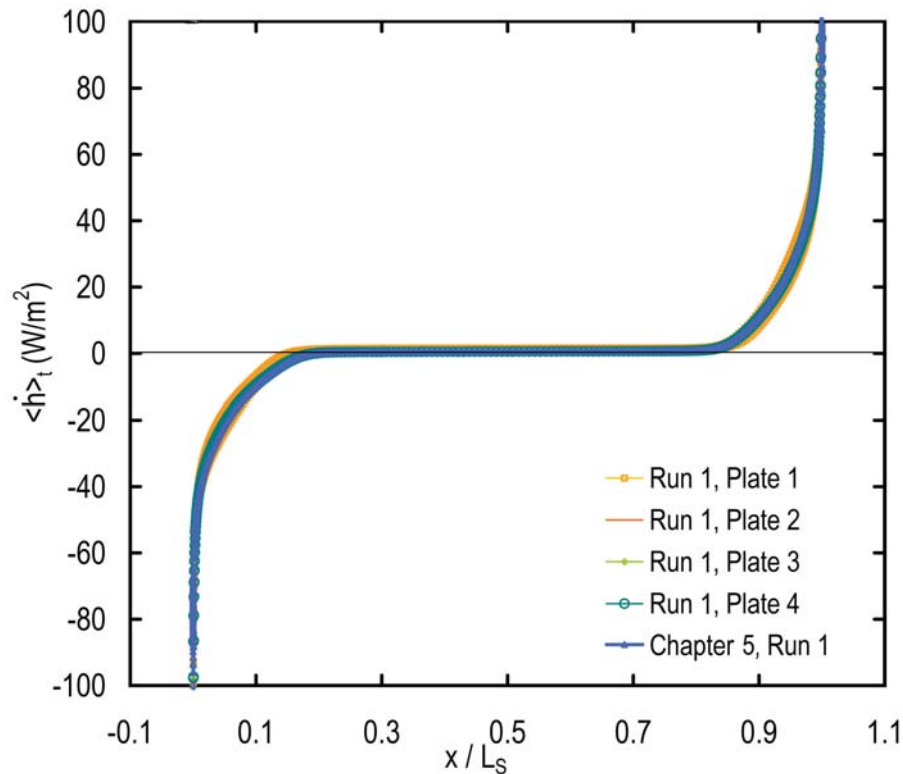
Figure 6.11: Distribution of the time-averaged heat flux for all four plates of Run 1 and Run 1 of Chapter 5. Mean pressure p_m is 0.1 bar.

in acoustic streaming through the pore adjacent to this face may be responsible for the increase in time-averaged transverse heat flux. Results obtained on all other stack faces exhibit similar heat transfer rates to Run 1 in Chapter 5.

Figures 6.13(a) and 6.14(a) present the time-averaged heat flux for Runs 3 (DR=1.7%) and 4 (DR=3.4%) respectively. Further to these two graphs, Figures 6.13(b) and 6.14(b) show increased detail of the 'cold end' of the stack. Figure 6.14 includes data obtained from Run 4 of Appendix D.3, which considers the same operating conditions and materials but using a single plate model.

Figures 6.13 and 6.14 both show that the time-averaged heat flux across the stack plates has inherent bias between the plate edges, and that the upper surface of all four Stack Plates are demonstrated to generate higher rates of $\left\langle \dot{h}_y \right\rangle_t$.
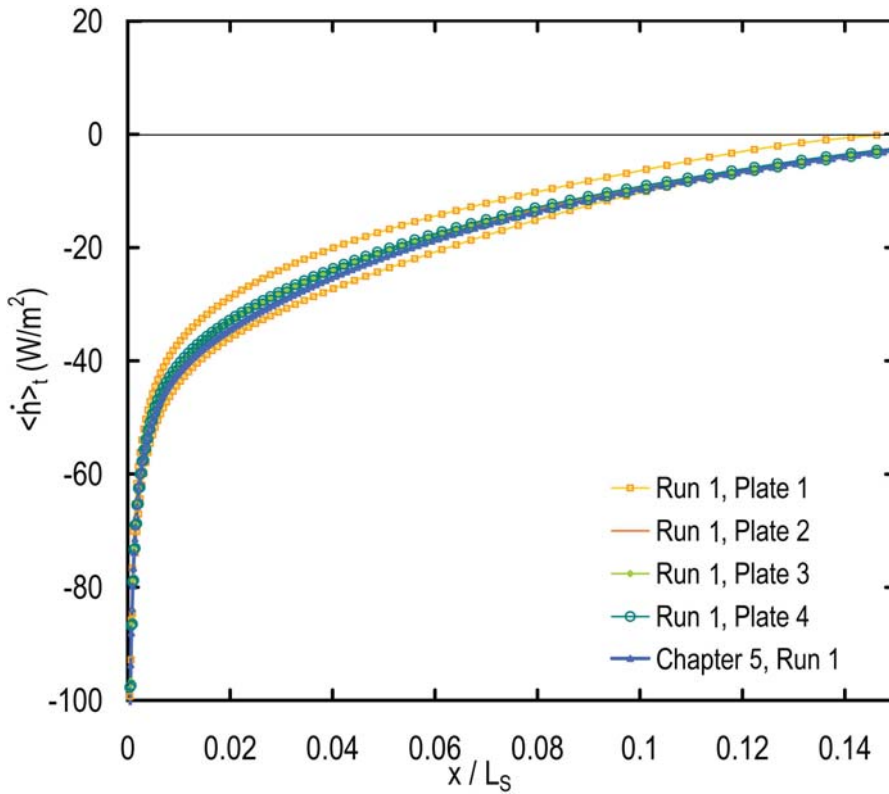
Figure 6.12: Distribution of the time-averaged heat flux as per Figure 6.11 showing increased detail on the 'cold' end of the thermoacoustic couple / stack region.

Stack Plate 1 is considered the most effective of all four Stack Plates in terms of effective cooling power, regardless of the mean pressure or drive ratio modelled, although the performance gain is modest. For Run 3, the cooling power $\dot{Q}_{S,cold}$ evaluated for Stack Plate 1 was approximately 3% greater on average than the other three plates, and for Run 4, only 2% more effective. This improvement is expected to be due to that fact that Stack Plate 1 is located nearest to the resonator wall where acoustic streaming is relatively minimal, as indicated in Figures 6.9 and 6.10.

The value of $\left\langle \dot{h}_y \right\rangle_t$ for the single plate model (Run 5 of Appendix D.3 of Chapter 5) is shown in Figure 6.14(b) to be less than that obtained on the lower side of Stack Plate 4 in Run 4, but greater than that obtained on the upper side. It has been demonstrated that the presence of acoustic streaming in Runs 5 and 6 has resulted
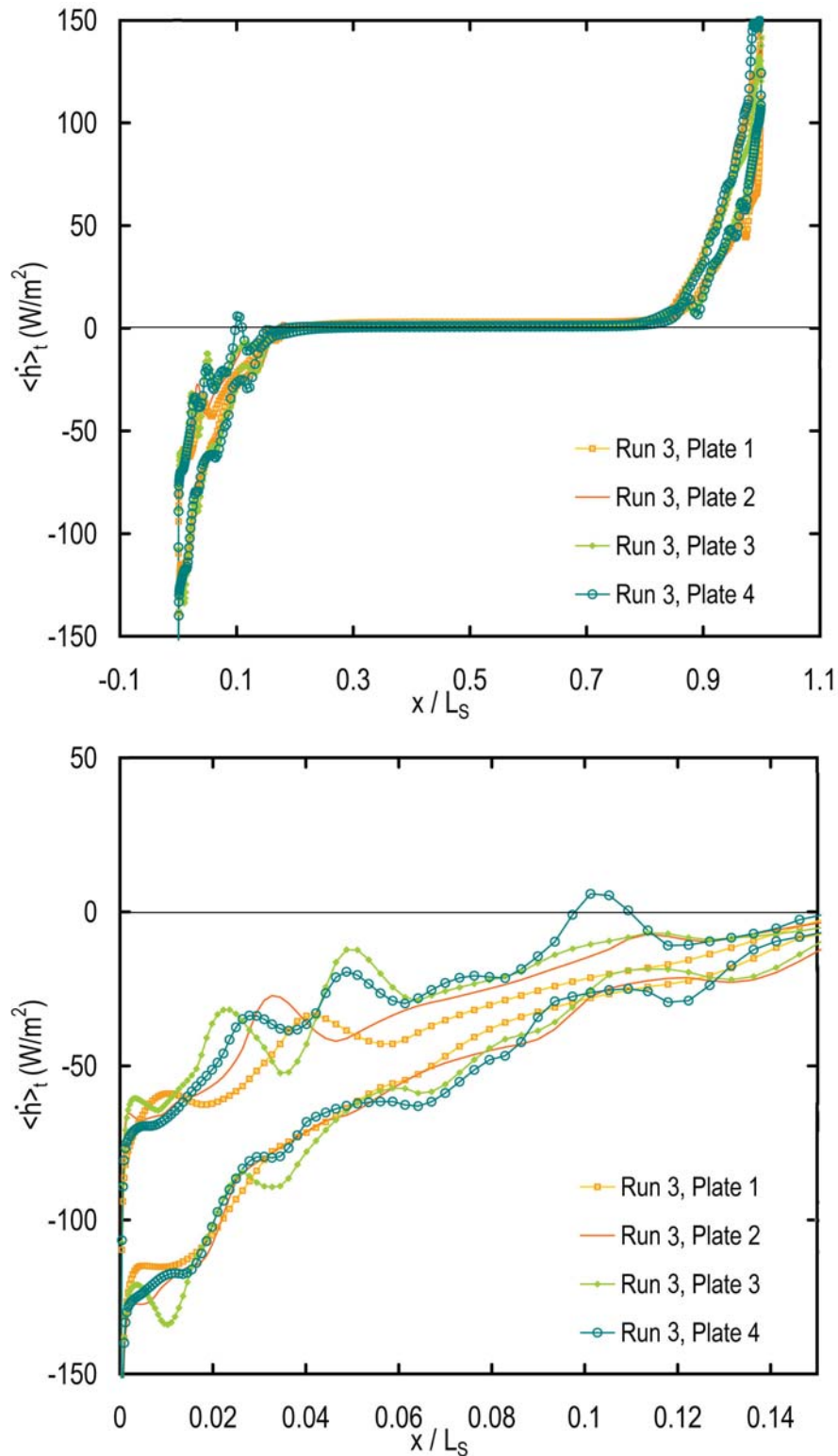
Figure 6.13: (a) Distribution of time-averaged heat flux in the y-direction $\left\langle \dot{h}_y \right\rangle_t$ along the horizontal plate surface according to axial position x for Run 3. $p_m=1$ bar, $DR=1.7\%$. (b) Increased detail of (a) near the 'cold end of the stack.
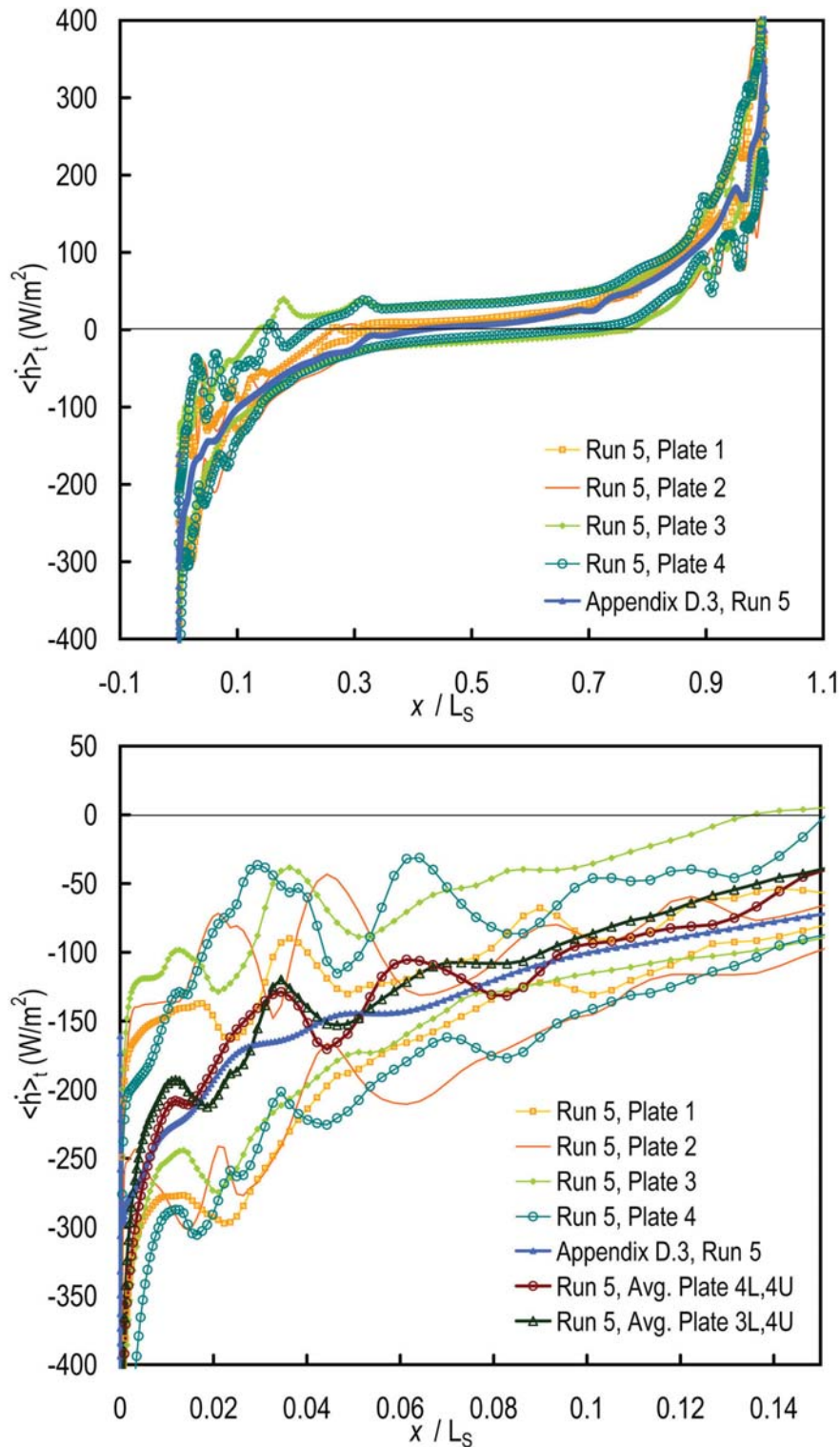
Figure 6.14: (a) Distribution of time-averaged heat flux in the y-direction $\left\langle \dot{h}_y \right\rangle_t$ along the horizontal plate surface according to axial position x for Run 4. $p_m{=}1$ bar, $DR{=}3.4\%$. (b) Increased detail of (a) near the 'cold end of the stack. The arithmetic average of both upper and lower sides of Stack Plate 4, and the arithmetic average of the lower surface of Stack Plate 3 and upper surface of Stack Plate 4 are also plotted.

in flow conditions which are not able to be captured using Run 5 of Appendix D.3. Regardless, the distribution of $\left\langle \dot{h}_y \right\rangle_t$ for Run 5 of Appendix D.3 appears to be close to the mean of $\left\langle \dot{h}_y \right\rangle_t$ obtained from both the upper and lower surfaces of Stack Plate 4 for Run 4, and the plate surfaces spanning the gap between Stack Plates 3 and 4.

6.2.3   Temperature fields

Figure 6.15 presents contour plots of mean temperature for Runs 3 to 5, and shows the increase in temperature gradients with increasing drive ratio. The spatial distribution of $\langle T_k \rangle_t$ is small for this drive ratio, but there are two noticeable trends: minima and maxima in $\langle T_k \rangle_t$ develop on the stack plate *edges*; and large regions upstream and downstream of the stack region are at different temperatures and have significant temperature gradients in the *transverse y* direction. For Run 4, it can be clearly seen that mean temperature distributions within adjacent stack pores are not the same. Instead, an 'alternating' pattern is shown to have developed. It can be seen that the mean temperature distribution is not uniform across the stack for all runs using a mean pressure of 1 bar.

Figures 6.15(b) and Figure 6.15(c) show variation in temperature profiles between pairs of stack plates. The variation in temperature profiles between channels or pairs of stack plates is expected given the identification of acoustic streaming for Runs 4 and 5 in Section 6.2.1. Acoustic streaming in the regions between Stack Plates 1 and 2, and between Stack Plates 3 and 4, was found to circulate contrary to the free-stream flow in Section 6.2.1. In other words, acoustic streaming effects lead to gas moving in the opposite direction to that intended, and this spoils the required phasing for effective heat transportation. This is evident in Figures 6.15(b) and Figure 6.15(c), where the temperature at the 'cold' end of the stack is higher in the region between Stack Plates 1 and 2 and also between

Stack Plates 3 and 4. Acknowledging that for Run 5, significant non-linear effects are likely to be present or that the transition to turbulence has occurred, the result shown in Figure 6.15(c) is nonetheless similar to that obtained in Figure 6.15(b) with regard to demonstrating this phenomenon.
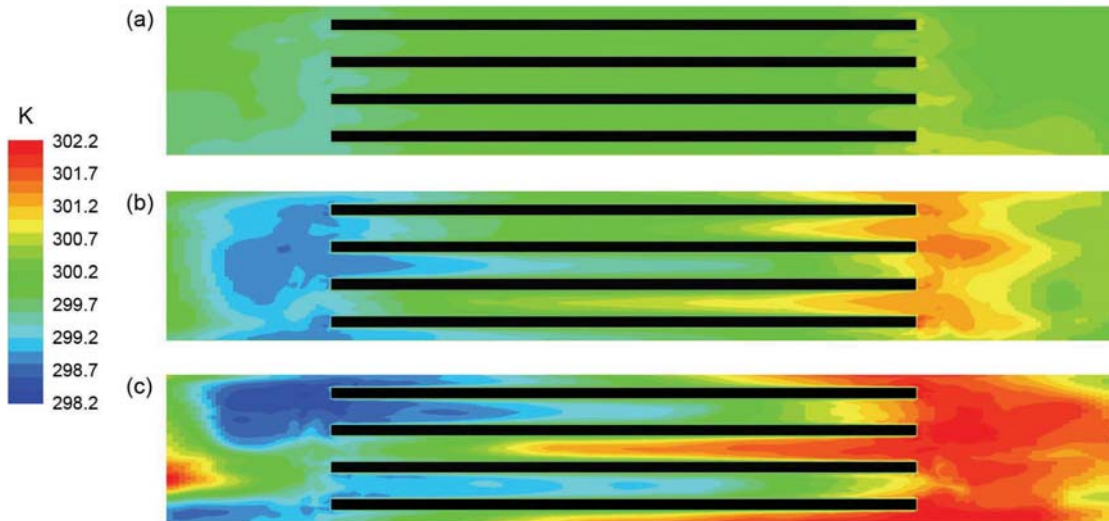

Figure 6.15: Contours of mean temperature for increasing drive ratio. (a) Run 3, DR=1.7%, (b) Run 4, DR=3.4%, (c) Run 5, DR=5.1%.

Figure 6.16 presents the COP (defined in Equation (5.10)) of the stack region for Runs 3 to 8. Setting the plate thickness t_s equal to the mean thermal penetration depth $\delta_{\kappa m}$ is here shown to produce more effective performance results than for $t_s/\delta_{\kappa m}$=3.2 as per Runs 3 to 5.

6.3 Summary and conclusions

To address the fourth 'gap' identified in Section 2.4, that time-averaged gas flow within parallel-plate thermoacoustic stacks has not been fully investigated, a multiple stack plate model is introduced and is shown to be capable of modelling acoustic streaming localised to the stack plates. It is shown that large scale vortices
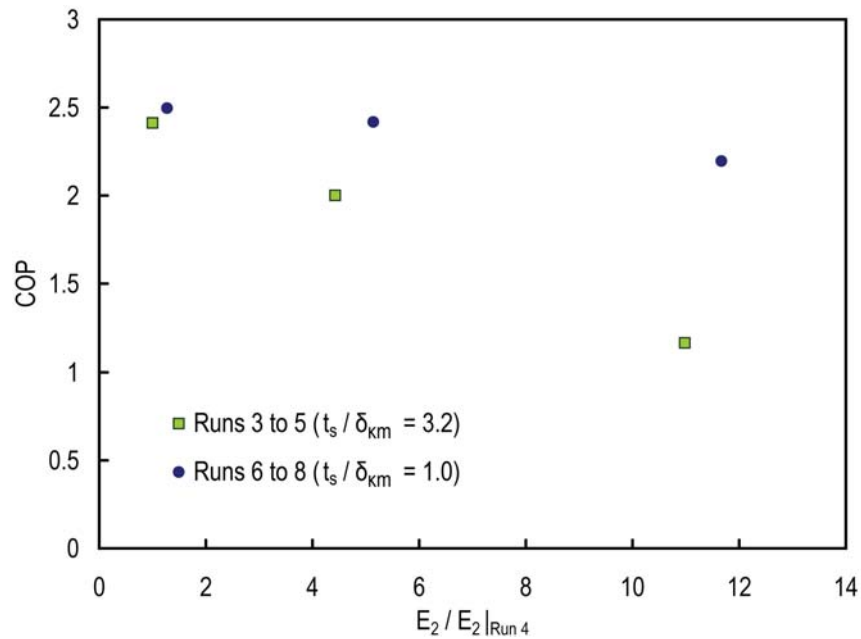
Figure 6.16: COP for normalised acoustic power input using the results of Runs 3 to 8.

are generated of a scale similar to the transverse width of the computational domain, and smaller scale vortices similar in size to the width of stack pores are shown to develop upstream and downstream of the stack region. It is shown that the time-averaged non-zero flow paths, which increase the mean velocity in several of the stack channels but retard flow in other channels, adversely affect the time-averaged temperature distribution.

At a mean pressure of 0.1 bar and low drive ratio, where acoustic streaming is not evident, the time-averaged heat flux evaluated at the plates near the central axis of the resonator in the multiple stack plate model is nearly equal to the same result obtained using the single plate model. Where acoustic streaming is evident, particularly for the runs where the drive ratio was 3.4% and 5.1%, the time-averaged heat flux is non-uniform amongst plates or between pairs of upper and lower surfaces on individual stack plates, however the same result obtained using the single plate model closely approximates the mean value between the upper and lower surfaces of the plate located nearest the central axis of the stack.

The numerical model presented in Chapter 3 and Appendix B does not consider acoustic streaming, a phenomenon shown in this Chapter to influence the performance of thermoacoustic couples, but it remains an effective tool for detailed investigation of the complex flow and temperature fields associated with practical thermoacoustic couples. The expanded thermoacoustic couple model is shown to be effective for the identification of conditions for which acoustic streaming is likely to occur.

Chapter 7

Conclusions and future work

Outcomes from this thesis and future research opportunities are discussed in Sections 7.1 and 7.2 respectively.

7.1 Conclusions

A numerical model was developed using the computational CFD code *Fluent* to provide new information regarding the flow, heat and temperature fields in thermoacoustic couples. Analysis of the model showed excellent agreement with results from previous numerical studies in this field (Cao et al. 1996, Ishikawa 2001, Piccolo & Pistone 2006). The error analysis (presented in Appendix B) considered the impact of grid mesh density, various solver models and levels of discretisation, temporal discretisation and extended time scales. The results of the error analysis gave confidence to proceed with the numerical studies presented in Chapters 4, 5 and 6.

Using this model, the performance of thermoacoustic couples was investigated with respect to increasing plate thickness, differing edge shape profiles and conditions affecting time-averaged acoustic streaming. Flow structures within the thermoacoustic device were also studied to assist the understanding of the complex flows

and resultant heat transfer, especially at higher drive ratios.

7.1.1 Effect of blockage ratio

Thermoacoustic couples of zero and finite thickness were compared in terms of the flow structure and rate of heat transportation for specified drive-ratios up to 6.8%. This comparison presented in Chapter 4 concluded that flow impedances from non-zero thickness stack plates and other fixed objects in the acoustic field will introduce flow and heat transportation characteristics previously unseen in earlier numerical studies of zero-thickness thermoacoustic couples. Results from Chapter 4 indicate that the blockage ratio (BR) strongly controls the generation of vortices outside the stack region and perturbs the flow structure and heat flux distribution at the extremities of the plate. Reductions in BR through increases in plate thickness t_s were also shown to improve the integral of the total heat transfer rate but at the expense of increased entropy generation and lower efficiency.

7.1.2 Effect of stack plate edge profile

Four variants of stack plate edge profile were compared to the conventional representation of thermoacoustic couples as a rectangular profile. The flow structure and rate of effective heat transfer were examined. The conventional rectangular profile of a stack plate with a blockage ratio of 0.7 was modified with rounded, 'aerofoil', bulbous and 'talon' shaped edges. The effectiveness of each edge shape profile was compared at various drive-ratios up to 6.8%.

It was found that the stack plate edge shape controls the overall performance of the thermoacoustic couple. At a drive ratio of 1.7%, the more bluff edge shapes were found to perform more desirably. At drive ratios of 3.4%, 5.1% and 6.8%, the sleeker edge shape profiles were more efficient. Only the Rounded edge shape profile was identified to be more efficient than the Rectangular edge shape for all

drive ratios invesigated.

Results from this study indicate that rounding the edges of a rectangular stack section yields improvements in the effective cooling rate and COP. Rounding the edges minimises the formation of gas recirculation zones downstream of each stack plate edge and hence improves the COP.

7.1.3   Time-averaged acoustic streaming in a multiple stack plate model

A multiple stack plate model was developed in Chapter 6 using an expanded domain to that presented in Chapter 3 with consideration of atmospheric mean pressure and materials common to thermoacoustic engines and refrigerators. The domain was expanded in the transverse direction to the flow, such that four entire plates and a side wall were included in each simulation.

The multiple stack plate model was shown to be capable of capturing time-averaged mass streaming or 'acoustic streaming' localised to the stack plates. Vortex generation of larger scales similar to the transverse width of the resonator, and at smaller scales similar in size to the width of stack pores were shown to develop upstream and downstream of the stack region. Time-averaged non-zero flow paths which increase the mean velocity in several of the stack channels but retard flow in other channels was shown to adversely impact upon the time-averaged temperature distribution. The expanded thermoacoustic couple model was found to be effective in the identification of conditions for which acoustic streaming is likely to occur.

The publications resulting from this thesis are listed in Appendix E.

7.2   Recommendations for future work

7.2.1   Improving the detail of the numerical model

The complexity and detail of the numerical model used in this study was set to the highest levels that could be afforded on the computing resources available. Details regarding the computing clusters available and used in this study are provided in Appendix C.

Ideally, the numerical model should be capable of resolving both the fine detail of a whole thermoacoustic stack region and the broader external boundary regions, accounting for turbulent and compressible flow characteristics of high amplitude sound oscillations over timeframes of the order of minutes. This should eventually be possible with continual growth in the speed and capacity of available computing resources.

The computational efficiency of the model can be further improved through use of an automatic grid mesh adaption tool such as that included in the *Fluent* CFD software.

7.2.2   Simulation of very high drive ratios

The numerical model presented in this thesis was developed to model steady and unsteady laminar flows only, and compliance with the criterion $N_{R,S} \leq 40,000$ ensured that the model was capable of adequately representing the physical flow field. Use of more complex turbulence models will allow flows with higher $N_{R,S}$ values to be simulated, meaning that the performance of highly pressurised thermoacoustic systems with high drive-ratios may be predicted using a higher-order numerical model.

7.2.3 Treatments for acoustic streaming

It should be relatively straightforward to investigate stack plate treatments to address the time-averaged mass streaming near the edges of each stack plate (Chapters 4 and 5) and in loops around each plate (Chapter 6). The study presented in Chapter 5 did not investigate whether combinations of stack edges (e.g. one edge 'Rounded', the other 'Aerofoil' or 'Rectangular') would have improved the performance of the stack plate. The 'Rounded' edge shape profile was found to reduce flow separation immediately downstream of each stack plate edge, so rounding the edges of stack plates in the multiple stack plate model may reduce the rate of flow instability created by jet streaming. Swift (2002, Section 7.4.2) suggests that suitable tapering of the resonator walls may suppress Rayleigh streaming.